Quantum Science and
Technology

PAPER • **OPEN ACCESS**

Tuning of quantum dots in micropillar cavities for hybrid photonic interfaces

To cite this article: Esteban Gómez-López *et al* 2026 *Quantum Sci. Technol.* **11** 025021

IOP Publishing Quantum Sci. Technol. 11 (2026) 025021 https://doi.org/10.1088/2058-9565/ae4d00

Quantum Science and Technology

OPEN ACCESS

RECEIVED
14 November 2025

REVISED
10 February 2026

ACCEPTED FOR PUBLICATION
3 March 2026

PUBLISHED
13 March 2026

PAPER

Tuning of quantum dots in micropillar cavities for hybrid photonic interfaces

Esteban Gómez-López[1,*], Moritz Meinecke[2], Karol Winkler[2], Jonathan Jurkat[2],
Tobias Huber-Loyola[2,3], Sven Höfling[2] and Oliver Benson[1]

[1] Institut für Physik, Humboldt-Universität zu Berlin, 12489 Berlin, Germany
[2] Technische Physik, University of Würzburg, 97074 Würzburg, Germany
[3] Institute of Photonics and Quantum Electronics, Karlsruhe Institute of Technology, 76131 Karlsruhe, Germany
[*] Author to whom any correspondence should be addressed.

E-mail: egomez@physik.hu-berlin.de

Keywords: quantum dots, micropillars, wavelength tuning, hybrid interfaces, single photon sources

Supplementary material for this article is available online

Abstract

Hybrid quantum interfaces that combine the fast, deterministic single-photon emission of semiconductor quantum dots (QDs) with the long-lived quantum memories of atomic vapors represent a promising route towards scalable quantum networks and distributed quantum computing. However, the realization of such interfaces is fundamentally limited by the stringent spectral matching required between the narrow optical transitions of atomic systems and the intrinsically variable emission of QDs. Moreover, achieving bright QD emission requires integration into an efficient light-collecting structure. In this work, we present a systematic investigation of three tuning mechanisms for cavity-enhanced QDs embedded in micropillar cavities: thermal tuning, *in situ* laser processing, and nitrogen gas deposition. We experimentally evaluated the applicability of each method and characterized their tuning ranges and precisions. All three methods enable reliable and precise wavelength shifts, even for QDs in larger micropillars. These results provide practical strategies for achieving spectral resonance between QD emitters and atomic vapor lines, paving the way for tunable solid-state-atomic hybrid platforms for photon storage, synchronization, and interfacing in hybrid quantum systems.

1. Introduction

Photonic qubits serve as fundamental building blocks for next-generation quantum technologies, enabling both quantum communication networks and photonic quantum computing architectures [1, 2]. The realization of practical photonic quantum systems requires high-quality, on-demand single-photon sources capable of generating indistinguishable photons with deterministic timing [3, 4]. Semiconductor quantum dots (QDs) have emerged as leading candidates for such applications, offering several compelling advantages over spontaneous processes such as parametric down-conversion [5, 6]. QDs provide bright, on-demand single-photon emission with exceptionally low multi-photon contributions, high indistinguishability, and precise temporal control [7, 8]. When embedded in optical microcavities like micropillars with distributed Bragg reflectors (DBRs), these sources achieve near-transform-limited emission with improved collection efficiency through the Purcell effect [9–12]. Additionally, placing QDs in optical cavities helps suppress the phonon sideband, further enhancing indistinguishability [13, 14].

Hybrid quantum interfaces that combine the complementary strengths of different quantum systems present exciting opportunities for advanced quantum technologies [15]. The integration of solid-state QDs with atomic vapor systems is particularly promising, as it merges the deterministic, high-rate photon generation capabilities of semiconductors with the long-lived quantum memories [16] and precise spectral references provided by atomic ensembles [17]. Atomic vapors can serve multiple functions in such hybrid systems, including quantum memories for buffering photonic qubits and performing synchronization operations [16, 18], precise frequency references for stabilizing emission wavelengths [19], and platforms for implementing slow light and storage protocols [19–22]. These hybrid architectures are essential for quantum repeater networks [18, 23, 24] and distributed quantum computing applications [25, 26].

Recent experimental efforts have demonstrated the feasibility of interfacing QDs with atomic systems, though significant challenges remain. Previous works have shown 'slow light' effects in which QD-generated single photons are delayed in atomic cesium vapor, preserving their quantum properties while extending interaction times [19, 20, 27]. Most recently, researchers have developed electromagnetically induced transparency (EIT) quantum memories in warm cesium vapor specifically designed to store QD-generated photons, with measured bandwidths approaching the Fourier-limited emission characteristics of cavity-enhanced QDs [21, 22].

However, the precise spectral matching required for efficient hybrid operation presents a bottleneck for further applications. QDs exhibit inherent wavelength variations due to size and composition fluctuations during growth, while atomic transitions provide fixed spectral references with sub-GHz precision [19, 27]. Different *in situ* approaches have been performed to tune QDs in optical cavities. Thermal tuning of QDs is a widely used approach to tune QDs to resonance with optical cavities [9, 28, 29]. Furthermore, strain tuning of μ-pillar cavities, performed by applying a controllable strain to the cavity, has been demonstrated in short pillars, which limits the performance of the cavity [30]. Additionally, *in situ* laser processing (ILP) has been used to tune QDs and microdisk cavities, where a strong laser is used to heat the cavity locally [31]. Furthermore, the deposition of gases on the surface of the photonic cavities has been utilized to induce a shift in the resonance of the cavity and to couple QDs to the cavity at a constant temperature, without tuning the QD wavelength. Deposition of neon and xenon gases has shown a shift of 4 nm in photonic crystal slab nanocavities [32, 33] and microdisk cavities [34]. A combination of ILP and gas deposition has been utilized to achieve reversible tuning of nanowire QDs, enabling interfacing with atomic vapors [35]. Micropillar-embedded QDs (μ-pillar QDs) represent a particularly well-suited architecture for hybrid quantum interfaces due to their ease of fabrication and optical emission quality [9, 10, 36]. However, the encapsulation of QDs in this architecture shields them from the environment, limiting the applicability of some tuning strategies.

This work investigates the application of thermal, ILP and nitrogen deposition tuning techniques to micropillar QDs, as illustrated in figure 1(a), with the objective of achieving bright, mode-matched emission and precise spectral alignment with narrow atomic resonances, without the need for any post-fabrication technique of the μ-pillar QD sample. Despite the relatively large μ-pillars, protected with planarizing benzocyclobutene (BCB) polymer, we demonstrate the effectiveness of the three mechanisms for frequency control, with ILP enabling coarse adjustments over a broad spectral range and thermal as well as nitrogen-deposition tuning providing fine control suitable for resonant matching, for instance, to individual hyperfine transitions in Cs atoms.

2. Method

QDs embedded in μ-pillar cavities

The μ-pillar QDs studied in this work are prepared following the process described in [9]. Employing molecular beam epitaxy, a wafer of gallium arsenide (GaAs) is grown, followed by a series of intercalated layers of GaAs and aluminum arsenide (AlAs), each quarter wavelength thick, to form a DBR. The bottom part of the DBR consists of 35 layers. A wavelength thick layer of indium arsenide (InAs) is deposited as active medium, followed by the top 15 layers of the DBR, as shown in figure 1(b). Pillars with diameters from 1 to 8 μm are defined via electron beam lithography and etched using electron-cyclotron-resonance reactive-ion-etching. The sample is then planarized with BCB. The BCB polymer is spin-coated and ashed to correct the height after curing at high temperature.

The μ-pillar QDs sample is placed in a continuous flow cryostat (Cryovac) and cooled down with liquid Helium. A simplified schematic of the experimental setup is shown in figure 1(c). The μ-pillars are excited with an off-resonant laser at 532 nm using a high numerical aperture microscope objective, NA $= 0.80$. The micro-photoluminescence (μ-PL) is collected and filtered using a confocal microscope in 4f-configuration. The off-resonant excitation light is suppressed by 50 dB using a 850 nm long-pass filter. The μ-PL spectra are collected using a spectrometer (Acton Research, SP2500) and detected with a charged-couple device camera (Oxford Instruments, iDus 420). To confirm the detected μ-PL is coming from a single QD, a spectral line is selected using a narrow band-pass filter, 1 nm bandwidth, and sent to a fiber-based Hanbury-Brown–Twiss setup (HBT). The HBT consists of a 50:50 beam splitter and

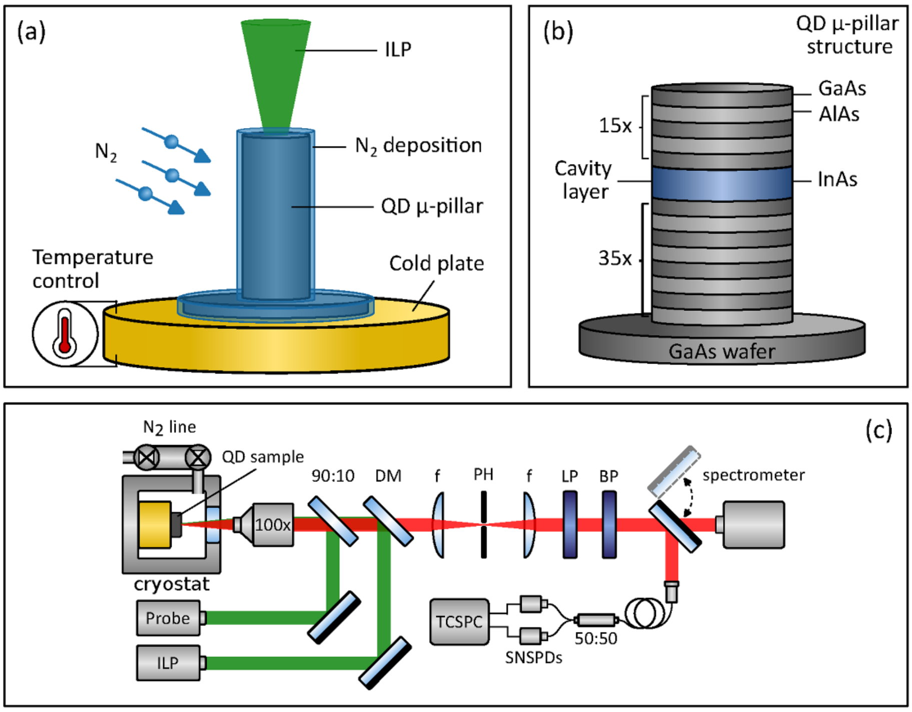

Figure 1. Post-fabrication tuning of quantum dots embedded in μ-pillar cavities. (a) Schematic of the investigated tuning mechanisms, thermal tuning, *in-situ* laser processing (ILP), and nitrogen deposition on the surface of the pillar. (b) Layout of the μ-pillar QD. The cavity is formed as a GaAs/AlAs distributed Bragg reflector with an embedded low-density layer of In(Ga)As QDs. (c) Experimental setup. The sample is off-resonantly excited with a probe laser using a confocal microscope. The micro-photoluminescence (μ-PL) spectra are recorded continuously with a spectrometer. ILP is performed with a high-power off-resonant laser. Nitrogen is inserted using the cryostat vacuum line with a fixed volume and pressure in several cycles (DM: dichroic mirror, f: aspheric lens, PH: pinhole, LP: longpass filter, BP: bandpass filter, SNSPDs: superconducting nanowire single-photon detectors, TCSPC: time-correlated single photon counting).

two superconducting nanowire single-photon detectors (single quantum). The arrival times are autocorrelated using a time-correlated single photon counting module (PicoQuant, PicoHarp 300). The temperature of the cold plate is constantly monitored and stabilized during the experiment using a heater on the cold plate, which is regulated with a PID controller. The thermal stability achieved in the system is ± 100 mK around the set temperature of 10 K. A scanning electron microscope image of the μ-pillars after planarization is shown in figure 2(a). A detailed inspection of several pillars reveals an air gap between the BCB polymer and the pillars, as shown in figures 2(b) and (c).

Two μ-pillars of diameters 2.3 μm and 2.4 μm with the characteristic μ-PL spectra of QDs were identified, QD-A and QD-B. The quality factor (Q-factor) of these pillars is calculated from the measured spectra as $\lambda/\Delta\lambda$, where λ is the measured cavity wavelength and $\Delta\lambda$ is the cavity emission full width at half maximum. The resulting Q-factors for QD-A and QD-B are $Q = 1853(53)$ and $Q = 1910(13)$, respectively. The exciton (X) and biexciton (XX) lines of QD-A were identified, while only the X-line was located for QD-B. The excitonic lines of each QD are selected using a narrow-band-pass filter. From the recorded counts in the spectrometer (5 s integration time), and the measured end-to-end efficiency of our setup, 5%, we have a peak brightness for the X-lines at 10 K of 3400 cts s^{-1} for QD-A and 10 400 cts s^{-1} for QD-B. This corresponds to a calculated brightness at the first lens of 68 000 cts s^{-1} and 208 000 cts s^{-1}, respectively. A detailed discussion of the experimental conditions, the sample layout and the QD distribution is given in the supplementary information.

The autocorrelation function $g^{(2)}(\tau)$ is measured using the fiber-based HBT and displayed in figures 2(d) and (e). The data is fitted with an exponential function, and the linewidth is calculated following [36]: $g^{(2)}(\tau) = 1 - (1 - g^{(2)}(0))\mathrm{e}^{-\gamma|\tau|}$, with $1/\gamma$ the exciton transition linewidth. The obtained linewidths for QD-A and QD-B are $\gamma = 3.5(2)$ GHz and $\gamma = 2.8(1)$ GHz, respectively. These results with $g^{(2)}(0) = 0.40(2)$ for QD-A and $g^{(2)}(0) = 0.22(3)$ for QD-B, respectively, confirm that both emitters are quantum light sources. It is noteworthy that the spatial position of QD-A is close to the edge of the pillar, located at $r_\mathrm{A} = 0.8(1)\,\mu$m from the center of the cavity, while QD-B is fairly in the center with $r_\mathrm{B} = 0.2(1)\,\mu$m of its own pillar, as illustrated in the insets of figures 2(d) and (e). The position of the QDs was determined by a confocal scan of the μ-pillars, where the uncertainty is given by the drift and hysteresis of the linear positioners that move the sample in our cryostat, measured to be 100 nm h^{-1}.

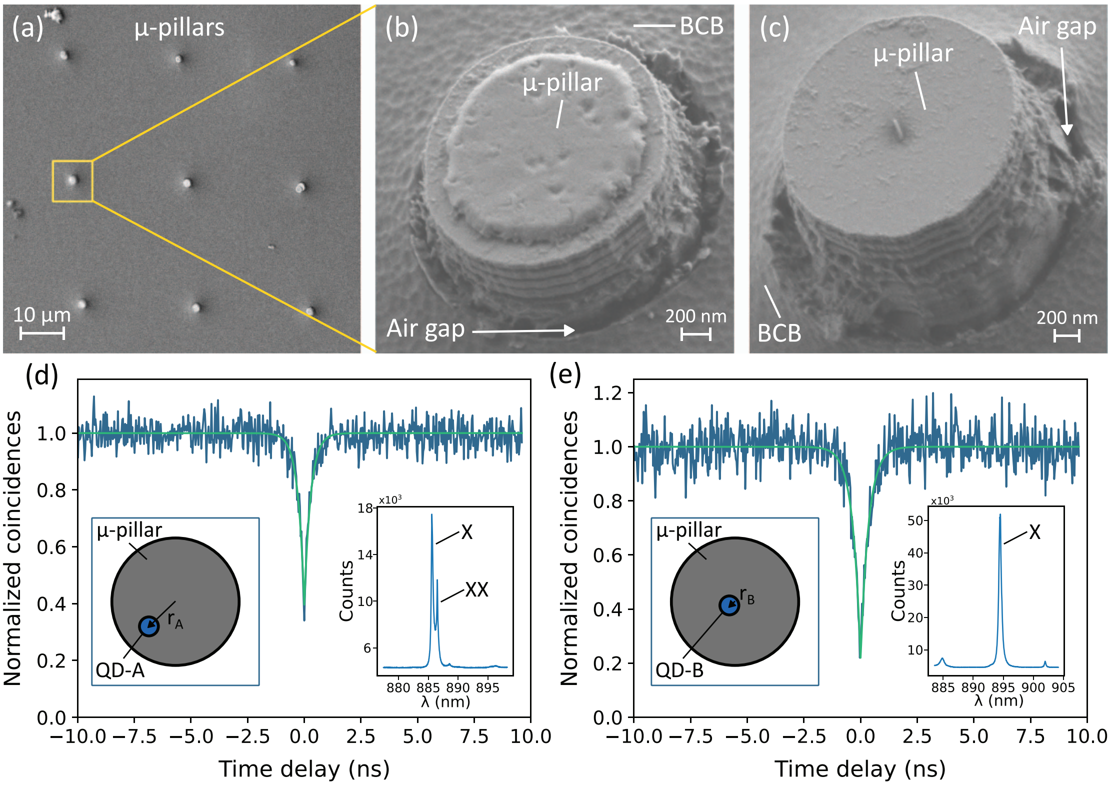

Figure 2. (a) Scanning electron microscopy of the μ-pillars on the sample after planarization with BCB polymer. (b), (c) Detailed image of two pillars with diameters 2.3 μm and 2.4 μm, respectively. An air gap is visible between the BCB and the walls of the pillars on all inspected pillars. (d), (e) Measured $g^{(2)}(\tau)$ in an HBT setup under non-resonant CW excitation of 19 μW for QD-A and QD-B. The measurements were performed on the exciton lines. The data is fitted with an exponential decay. Both QDs show a $g^{(2)}(0) < 0.5$, confirming the analyzed spectral lines are emitted by QDs. **Insets**: illustration showing the position of the QDs relative to the center of their respective μ-pillar. QD-A is located towards the edge of its pillar with $r_A = 0.8(1)\,\mu$m, whereas QD-B is located in the center of its cavity, $r_B = 0.2(1)\,\mu$m.

3. Results and discussion

3.1. Tuning of the emission lines

The emission lines of both emitters were tuned by applying three different tuning approaches: thermal tuning, which involved heating the sample via the heater on the cold plate; ILP, where a high-power laser was focused on top of each pillar; and nitrogen deposition, which involved inserting nitrogen gas into the sample chamber. The μ-PL spectra of both QDs under the different tuning processes are shown in figure 3. It is noteworthy that QD-B has an emission line, associated with the exciton transition, close to the cesium D_1 line at ~894.5 nm, making it of special interest for interfacing with this atomic vapor.

Thermal tuning

To perform the shift of μ-pillar QD spectral lines, the most straightforward mechanism is changing the temperature of the system comprised of QD and μ-pillar cavity. The shift of the QD emission and the cavity resonance originate from the temperature dependence of the energy bands and the refractive index, respectively [31, 37]. Increasing temperatures produce a reduction of the band-gap while increasing the refractive index of the μ-pillar cavity, resulting in a red shift of the μ-PL.

In our experiment, the temperature of the cold plate in the cryostat is stabilized at 5.0(1) K and the μ-PL spectrum of one of the QDs is recorded. The temperature is increased in steps of 0.5K, and after a thermalization time of 30 s, the subsequent spectrum is recorded. The resulting spectra are shown as a heatmap in figures 3(a) and (b) for QD-A and QD-B, respectively. As expected, the lines are red shifted with increasing temperature. In figure 3(c), we track the relative change of the X-lines of both emitters, that is, the difference of wavelength at different temperatures compared to the initial wavelength at 5 K, by fitting a Lorentzian curve to each row of the presented heatmaps. We perform a power law fit of the data, i.e. $\Delta\lambda = aT^n$, with a and n as free parameters. The errors reported in figures 3(c), (f) and (i) are

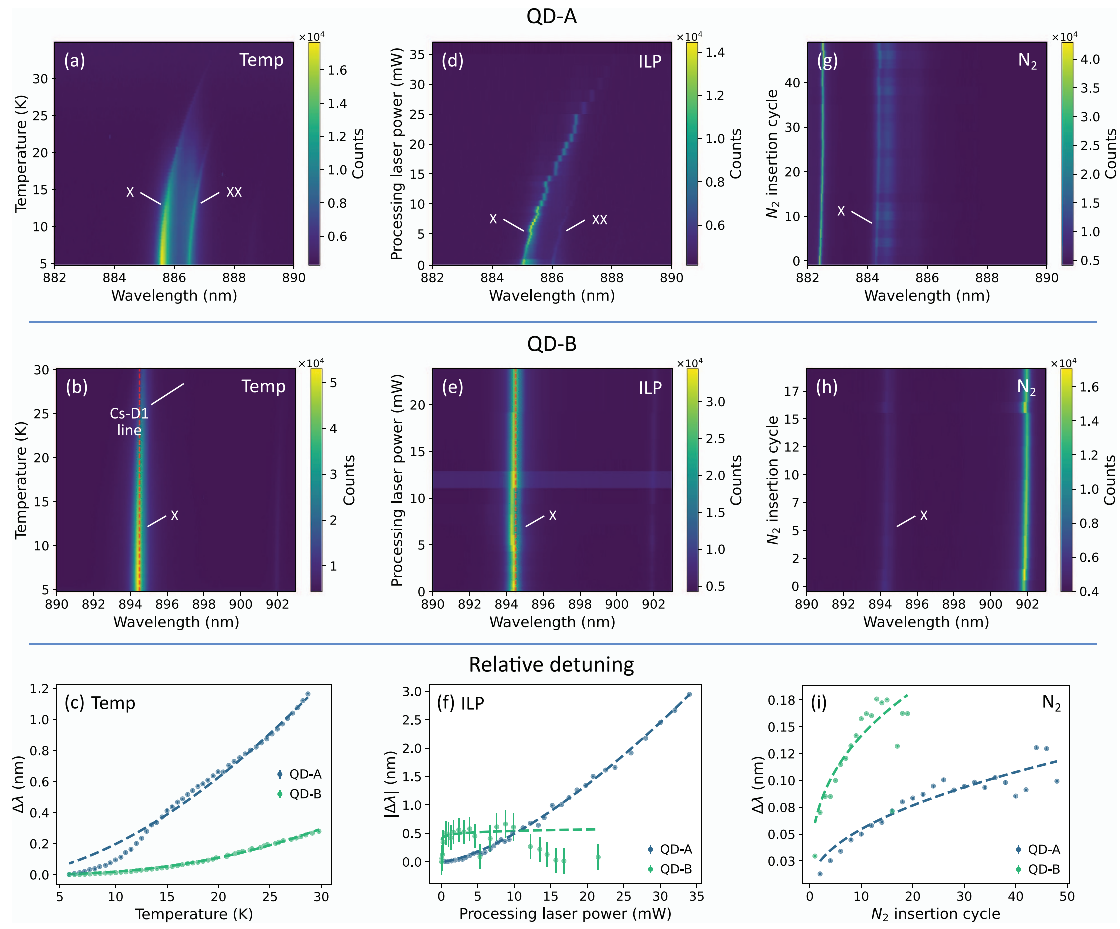

Figure 3. μ-PL spectra of two different QDs under the three distinct tuning processes. (a), (b) Thermal tuning: temperature variation of the μ-PL spectra by heating the cold plate of the cryostat. The Cs D_1 line is plotted as a reference for QD-B (red line). (c) Relative detuning $\Delta\lambda$ of the X-line of both QDs with varying temperatures. Both QDs are red shifted at different rates as discussed in the main text. Data fitted using power law functions of the form $\Delta\lambda = aT^n$ (dashed lines). **(d), (e) ILP tuning:** a 532 nm laser with increasing power is focused on each pillar, and the spectra are recorded after a 100 s exposure time per step. (f) $\Delta\lambda$ of the X-lines as a function of the laser processing power during the ILP. QD-A shows a significant tuning ($\sim$3 nm) while QD-B has no clear tendency, fluctuating around the starting wavelength. **(g), (h) Nitrogen deposition tuning:** a fixed amount of nitrogen is inserted into the cryostat per cycle, and the spectra are captured after thermalization of the sample chamber. **(i)** $\Delta\lambda$ of the same exciton lines with increasing N_2 volume per cycle. Tuning of both QDs is limited ($<$0.2 nm) and reaches a saturation. Notably, all tuning mechanisms produce a red shift on the μ-PL spectra of both QD-A and QD-B.

the standard deviation of the fit. Here, we can note different responses of both QDs, with QD-A being significantly more sensitive to thermal tuning, despite both being embedded in pillars with similar diameters and Q factors. This effect is not uncommon in self-assembled QDs and can be explained by the slightly different composition and local strain conditions created during the sample growth, given the statistical nature of the molecular beam epitaxy process, resulting in different thermal responses for each QD [38]. Thermal tuning offers the advantage of easy implementation and reversible detunings, albeit at the cost of reduced brightness and increased spectral broadening [39].

It is noteworthy that, despite being limited, thermal tuning of QD-B allowed the wavelength to shift across the Cs D_1 line at $\sim$894.5 nm. The Cs D_1 reference (red dotted line in figures 3(b), (e) and (h)) is obtained from the spectrum of a distributed-feedback laser diode locked to a Cs vapor cell using saturated absorption spectroscopy. This suggests that this QD could potentially be used for hybrid interfaces utilizing Cs vapor.

ILP

Following the thermal tuning, the sample is cooled down to 10 K and stabilized with the temperature controller, as a compromise between bright emission of both emitters and the helium consumption rate. A high-power laser (ILP laser) at 532 nm is overlapped with the probe laser using a dichroic mirror, as shown in figure 1(c). The power of the laser is monitored using the reflection of the 90:10 beam splitter, reaching a power density up to 9 W cm^{-2} for the highest ILP power used. The QDs are illuminated with a set processing power for 100 s of exposure time. Then, by blocking the ILP laser, the emitters

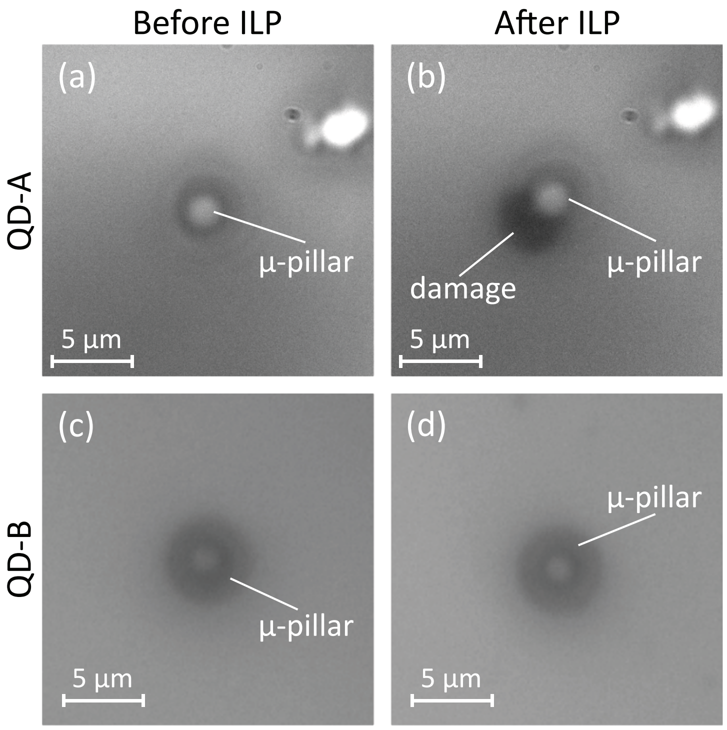

Figure 4. Wide field microscopy of QD-A and QD-B. (a), (b) QD-A before and after the ILP tuning was performed. The pillar with QD-A shows damage on its side caused by laser ablation during the ILP process. (c), (d) QD-B before and after ILP. The pillar with QD-B shows no visible damage due to the lower ILP powers used and longer thermalization between processing steps.

are excited using the probe laser with 19 μW of power, and the μ-PL spectrum is recorded. The process is repeated iteratively for progressively higher levels of processing power. Previous studies of QDs in microdiscs or in unstructured samples [31, 40, 41] have demonstrated a blue shift of the emission spectra at high laser processing powers. It was attributed to the intermixing of the QD material with the surrounding matrix when a temperature of 1000 K is reached.

Our resulting μ-PL spectra are presented as heatmaps in figures 3(d) and (e). Using the same analysis as in the case of thermal tuning, the shift of the excitonic lines of both QDs is tracked and plotted in figure 3(f) as relative detuning. There are two observations: first, QD-A exhibits a large tuning range, achieving a 3 nm red shift, whereas QD-B shows almost no response. Second, instead of the expected blue shift from intermixing, we observed a red shift in our experiments, even though we used optical powers similar to those reported in previous studies. We explain the first observation with different heating protocols for QD-A and QD-B, respectively. The spectra of QD-A were captured with no more than 5 s between the ILP process and the measurement of the spectrum, while for QD-B, the spectra were recorded 120 s after the ILP. This longer waiting time between ILP steps was mainly to prevent damage to the pillar, the QD and the surrounding BCB polymer due to heat accumulation. QD-A did not have sufficient time to thermalize after a single irradiation, causing heat to accumulate with each step, resulting in a significantly higher pillar temperature compared to QD-B. This buildup of heat damaged or partially ablated the surface of the μ-pillar and the surrounding BCB material, as shown by a closer inspection of the studied pillars before and after ILP (figure 4). Regarding the second observation, namely the red-shift, we note that QD-A was positioned off-center (as indicated in figure 2), closer to the pillar edge. We attribute the primary tuning mechanism in this case to a modification of the pillar–BCB interface induced by local heating without reaching the intermixing regime. Since QD-A is located near the edge, the confinement potential for the charge-carrier wavefunction is changed by this modification, whereas QD-B, situated at the center (and experiencing lower heating), remained unaffected. An important remark about the ILP approach is that once the ablation of the pillar occurs, the tuning process becomes irreversible. For QD-A, we observed a permanent red-shift of 1.68(3) nm after one hour of thermalization following the latest ILP step; see supplementary information figure 2. The ILP tuning approach for QD-A turned out to be reliable and provided a large tuning range, with a permanent red shift of up to 1.7 nm.

Nitrogen deposition

Finally, we explored tuning of the QDs by nitrogen N_2 deposition. To do this, we modified the vacuum line of our continuous-flow cryostat by adding a gas insertion line with a fixed volume of 92(5) ml, defined by the pipe between two high-vacuum valves, as shown in figure 1(c). The sample is cooled and stabilized at 10.0(1) K. The cryostat is then isolated from the vacuum pump. The insertion line is filled with 100 mbar of N_2 per cycle, which is then slowly released into the vacuum line. The temperature of the cold plate is monitored, and the flow through the valve is adjusted to keep it below 20 K. Once the pressure in the cryostat reaches a stable value, the system is left to thermalize for 120 s. We carefully made sure that this thermalization time was sufficient to reach the base temperature of 10 K again (see supplementary information figure 3). After each N_2 insertion cycle, the μ-PL spectrum is subsequently recorded. Figures 3(g), (h) and (i) show a red shift of the emission wavelengths for both QDs. Despite keeping the conditions as similar as possible, the initial pressure in the cryostat was slightly different for the measurement of QD-A and QD-B. This means that different amounts of frozen nitrogen were initially deposited on each QD, leading to the varying tuning ranges for each QD. Additionally, the nitrogen deposition tuning was performed a month after the ILP process. An initial blue shift of the X-lines for both QD-A and QD-B is observed (compare figures 3(d) and (e) with figures 3(g) and (h)), as well as a change in the relative brightness of the transition lines. This could be explained by the different strain conditions of the sample when it was placed in the cryostat and cooled down for each tuning process. Therefore, we focus mainly on the relative shifts of the X-lines.

It is noticeable that nitrogen deposition is effective for our sample, since the relatively large pillars are embedded in the BCB polymer. However, inspection of the SEM images displayed in figures 2(b) and (c) reveals gaps between the BCB and the pillars. Therefore, nitrogen can diffuse into these gaps and condense on the pillar surface.

In a cavity–QD system, nitrogen deposition can influence both the QD emission wavelength and the cavity resonance. The latter arises from modifications to the confining potential of the optical mode and is most pronounced for QDs embedded in photonic crystal cavities [32, 42] or microdiscs, where red shifts of up to 4 nm in the cavity resonance have been reported [34]. In our system, we investigate changes in the QD emission wavelength that originate from modifications to the confining potential of the charge-carrier wavefunction, induced either by geometric alterations or by strain effects [43]. This effect is particularly evident for QDs embedded in nanowires, where blue shifts on the order of ∼800 pm have been demonstrated, where the blue shift is attributed to compressive biaxial strain effects of the deposited nitrogen on the nanowire rather than compressive strain that would lead instead to a red shift as in our case [35]. Nanowires typically exhibit a base diameter of about 250 nm that gradually tapers to 100 nm at the tip [44], making the charge-carrier wavefunction especially sensitive to structural modifications at the rim of the wire. By contrast, our micropillars are substantially larger, approximately 4 μm in height with a diameter of ∼2.5 μm, which explains the significantly smaller maximum shift of ∼175 pm observed before saturation occurs.

An important observation of the nitrogen deposition technique developed here is its reproducibility and reversibility. Provided the temperature and pressure in the sample chamber remain stable, the nitrogen deposition process is reversible. This means that within a single cool-down cycle, the process is reversible; however, across different cooling cycles the tuning is not reproducible, given that the initial wavelength and tuning effect of the QDs vary slightly between cooling cycles. Here we remark that the data presented in figures 3(e) and (h) were recorded in two different cool-down cycles, showing the variation between cycles. In particular, the brightness of the exciton transition of QD-A varies from 1800 cts s^{-1} to 3600 cts s^{-1}; while QD-B varies from 1200 cts s^{-1} to 10 500 cts s^{-1} for two different cycles.

An advantage of tuning through nitrogen deposition is that the brightness of the QDs stays constant across the entire tuning range. This contrasts with the other two methods, where we observe spectral line broadening and a reduction in brightness. Despite this advantage, the maximum red-shift obtained was 0.175(1) nm for QD-B, as shown in figure 3(i), indicating a more limited tuning range compared to the temperature- and ILP-based approaches. Saturation occurs when no further nitrogen is incorporated into the structure or when any additional nitrogen no longer influences the QD environment.

Towards atomic-QD interfaces

As noted previously, QD-B is sufficiently close and can be tuned across the Cs D_1 line using our tuning methods. By heating the sample to 17 K, we have overlap with the emission line as shown in figure 3(b). In order to interface photons emitted from such a QD, not only must the emission wavelength match the atomic transitions, but also the linewidth of the QD photons and the atomic absorptions must be compatible. For a warm atomic vapor with sufficient optical density to perform an interfacing (80 °C for 40 mm vapor cells), the broadened absorption linewidths are ∼1 GHz [19]. Specific applications like

Table 1. Relevant optical properties, like autocorrelation $g^{(2)}(0)$, FWHM and brightness of the analyzed quantum dots. Figures-of-merit, range and precision, achieved for each tuning method investigated in this work. We compare our results with other interesting tuning mechanisms like AC and quantum confined Stark effects [47] and piezoelectric strain tuning [19]. It is important to note that our precision is currently limited by the thermal stability of our flow cryostat, which could be improved by an order of magnitude with a closed-cycle system.

		QD-A	QD-B	[35]	[19]	[47]
$g^2(0)$		0.40	0.22	0.130	0.02	—
FWHM	(GHz)	3.5	2.8	3.9	2.7	∼1
Brightness	(kcts s^{-1})	70	210	—	120	11
Thermal	range (nm)	1.16	0.28	—	—	—
	precision (nm)	0.05	0.01	—	—	—
ILP	range (nm)	2.94	—	∼0.250[a]	—	—
	precision (nm)	0.09	—	—	—	—
N2 deposition	range (nm)	0.130	0.180	∼0.830	—	—
	precision (nm)	0.003	0.008	∼0.003	—	—
Stark tuning	range (nm)	—	—	—	—	0.6
	precision	—	—	—	—	<0.0002
Piezo tuning	range (nm)	—	—	—	1.5	—
	precision (nm)	—	—	—	0.001	—

[a] In this work, [35], ILP was used for local heating of the nanowires to desorb deposited nitrogen rather than inducing laser ablation.

delay lines in the atomic ensembles can be implemented using photons with linewidths in the order of a few GHz, broader than the atomic transitions [19, 20]. For such slow-light interfaces, a precision and stability of ∼1 GHz of the emitted photons is sufficient. For more demanding applications, such as storage of photons in spin-wave excitations via EIT, a quantum memory, the acceptance window of the memory becomes a more limiting parameter. Room-temperature atomic vapor quantum memories can reach acceptance windows on the order of a few hundred MHz [45]. For highly efficient storage, the linewidth of photons must fit within this acceptance window [46]. Ideally, Fourier-limited single photons in the few hundred MHz range are desired, and tuning precision and stability on the order of the natural linewidth are required. Nevertheless, interfacing broadband photons with atomic vapors that have narrow acceptance windows is possible. In this scenario, the atomic vapor will act as a spectral filter. This relaxes the required precision and stability to a few GHz at the cost of interface efficiency and linewidth narrowing of the stored photons.

In our case, QD-B has an inhomogeneous linewidth of 2.8 GHz; consequently, only a fraction of the emitted QD light would interact with the atomic vapor, provided sufficient precision and stability are achieved through our tuning methods. Through the thermal tuning data, we calculate a sensitivity of 0.011 nm K^{-1}, equivalent to 4.12 GHz K^{-1} at 894.5 nm. The thermal stability of the system is measured to be ±100 mK with active temperature control, indicating that spectral diffusion is expected to be on the order of 400 MHz. Other works have demonstrated successful interfacing of QD light with atomic vapors, achieving similar stability: slow light through Cs vapor was demonstrated using piezoelectric strain-tuned QDs [19] and nanowire-QDs with reversible gas deposition tuning; additionally, quantum storage in a fast memory hosted in Cs was shown with thermally tuned CBG-QDs [21]. Given the similar ranges, precisions and linewidths used in the reported references, we confirm our μ-pillar QD can be successfully interfaced with Cs to create either a delay line using slow light or a quantum memory through spin-wave excitations in the atomic vapor. We summarize in table 1 the figures of merit: range and precision, achieved using our tuning methods, together with relevant optical properties like the autocorrelation $g^{(2)}(0)$ as a metric of photon number purity, FWHM and brightness of our analyzed QD devices. We also compare our parameters with other relevant works with distinct tuning mechanisms employed: reversible nitrogen deposition [35], piezoelectric strain tuning [19], and AC and quantum confined Stark effects [47].

Another aspect relevant to interfacing QD devices with atomic vapors is the excitation scheme. The linewidth of the QD will broaden using the above band excitation due to dephasing of carriers and carrier-photon scattering during the QD capture and emission process. Additionally, charge noise is increased significantly, leading to additional spectral diffusion [48]. Resonant excitation would provide near-transform-limited emission, allowing interfacing with systems with a narrow spectral acceptance window, such as quantum memories in atomic vapors [21]. Additionally, photon purity and indistinguishability could be increased to the reported values for this type of micropillar QD, $g^{(2)}(0) < 0.01$, and HOM visibility <0.1 [10]. The three tuning methods studied in this work (thermal, ILP, and nitrogen deposition) will drift on a much lower timescale than phonon- or carrier scattering. Therefore, the indistinguishability of emitted photons shall remain unaffected.

It is important to note that despite the benefits these tuning mechanisms offer, both ILP and nitrogen deposition would require the QDs to be located closer to the walls of the micropillar cavity, which is expected to reduce the Purcell enhancement factor [49]. A compromise between these tuning methods and the brightness of the observed μ-pillar QD is needed.

4. Conclusion and outlook

In this work, we investigated tuning of μ-pillar QDs, a widely adopted and robust photonic platform for efficient single-photon emission. We demonstrated that effective tuning can be achieved through a combination of reversible and irreversible processes. ILP enables red shifts of the emission wavelength over a broad range, up to 3 nm. However, the structural changes caused in the pillars at high ILP powers make this method irreversible, as well as lead to deterioration of the optical properties of the μ-pillars due to ablation. In addition, we showed that nitrogen deposition on the pillars can induce red shifts of the QD emission wavelength despite a large pillar size and BCB planarization. This technique is particularly suited for high-precision tuning over a narrower range and has the additional advantage of minimal spectral broadening. However, a limitation arises from the use of a continuous-flow cryostat, as in our experiment, which is sensitive to pressure variations and requires helium refilling, thereby reducing the practicality of deposition-based tuning, but it is widely applicable in closed-cycle systems. We further want to point out that both ILP and deposition tuning are more effective when QDs are located near the pillar rim. This implies a trade-off in structure design: maximizing brightness, narrow-linewidth emission, and near-Gaussian emission profiles must be balanced against achieving a large tuning range. Combining all three approaches, including thermal tuning, offers a pathway toward precise tuning of two remote QDs with respect to each other [50] for entangling them by photon interference, or toward hybrid interfacing of QDs with atoms [35]. Atomic vapors, such as Cs, represent practical quantum memories for quantum information processing and quantum network synchronization but are characterized by extremely narrow absorption lines (well below 1 GHz). This imposes a significant challenge for QD tuning in hybrid interfaces. The techniques presented here provide strategies for achieving the required tuning precision, thereby supporting the realization of semiconductor QD–atomic vapor interfaces.

Acknowledgments

This research received financial support from the free state of Bavaria, the German Research Foundation (DFG) under Project Number BE2224/19-1 and from the Federal Ministry of Research, Technology and Space (BMFTR) for Projects QR.N (16KISQ003, 16KIS2185) and MHLASQU (13N16029). THL acknowledges support from the BMFTR within Project Qecs (13N16272). The authors express their gratitude to technicians Monika Emmerling and Adriana Wolf for their contributions to sample fabrication, and to Sam Fairman for providing the SEM images.

Data availability statement

The data cannot be made publicly available upon publication because they are not available in a format that is sufficiently accessible or reusable by other researchers. The data that support the findings of this study are available upon reasonable request from the authors. https://doi.org/10.5281/zenodo.18299646 [51].

QD tuning supplementary available at https://doi.org/10.1088/2058-9565/ae4d00/data1.

Author contributions

EGL and OB conceived and designed the experiments. THL and SH designed the QD sample. MM, KW and JJ grew and processed the sample. EGL performed the experiments, analyzed the data, and wrote the manuscript with detailed discussions from OB, THL, and SH. All authors contributed to the manuscript, reviewed, and have approved the submission of the final version of the manuscript.

Conflict of interests

The authors declare no competing interests.

ORCID iDs

Esteban Gómez-López 0000-0002-8838-2888
Moritz Meinecke 0000-0003-1550-9080
Jonathan Jurkat 0000-0002-2313-7371
Tobias Huber-Loyola 0000-0002-5788-8501
Sven Höfling 0000-0003-0034-4682
Oliver Benson 0000-0003-4841-1231

References

[1] Kimble H J 2008 The quantum internet *Nature* **453** 1023–30
[2] Kok P, Munro W J, Nemoto K, Ralph T C, Dowling J P and Milburn G J 2007 Linear optical quantum computing with photonic qubits *Rev. Mod. Phys.* **79** 135–74
[3] Meyer-Scott E, Silberhorn C and Migdall A 2020 Single-photon sources: approaching the ideal through multiplexing *Rev. Sci. Instrum.* **91** 041101
[4] Uppu R *et al* 2020 Scalable integrated single-photon source *Sci. Adv.* **6** eabc8268
[5] Suprano A *et al* 2023 Orbital angular momentum based intra-and interparticle entangled states generated via a quantum dot source *Adv. Photon.* **5** 046008
[6] Lu C-Y and Pan J-W 2021 Quantum-dot single-photon sources for the quantum internet *Nat. Nanotechnol.* **16** 1294–6
[7] Uppu R, Midolo L, Zhou X, Carolan J and Lodahl P 2021 Quantum-dot-based deterministic photon–emitter interfaces for scalable photonic quantum technology *Nat. Nanotechnol.* **16** 1308–17
[8] Heindel T, Kim J H, Gregersen N, Rastelli A and Reitzenstein S 2023 Quantum dots for photonic quantum information technology *Adv. Opt. Photonics* **15** 613–738
[9] Unsleber S, Schneider C, Maier S, He Y-M, Gerhardt S, Lu C-Y, Pan J-W, Kamp M and Höfling S 2015 Deterministic generation of bright single resonance fluorescence photons from a Purcell-enhanced quantum dot-micropillar system *Opt. Express* **23** 32977–85
[10] Ding X *et al* 2016 On-demand single photons with high extraction efficiency and near-unity indistinguishability from a resonantly driven quantum dot in a micropillar *Phys. Rev. Lett.* **116** 020401
[11] Engel L, Kolatschek S, Herzog T, Vollmer S, Jetter M, Portalupi S L and Michler P 2023 Purcell enhanced single-photon emission from a quantum dot coupled to a truncated Gaussian microcavity *Appl. Phys. Lett.* **122** 043503
[12] Phillips C L *et al* 2024 Purcell-enhanced single photons at telecom wavelengths from a quantum dot in a photonic crystal cavity *Sci. Rep.* **14** 4450
[13] Grange T, Somaschi N, Antón C, De Santis L, Coppola G, Giesz V, Lemaître A, Sagnes I, Auffèves A and Senellart P 2017 Reducing phonon-induced decoherence in solid-state single-photon sources with cavity quantum electrodynamics *Phys. Rev. Lett.* **118** 253602
[14] Denning E V, Iles-Smith J, Gregersen N and Mork J 2020 Phonon effects in quantum dot single-photon sources *Opt. Mater. Express* **10** 222–39
[15] Chia C, Huang D, Leong V, Kong J F and Goh K E J 2024 Hybrid quantum systems with artificial atoms in solid state *Adv. Quantum Technol.* **7** 2300461
[16] Katz O and Firstenberg O 2018 Light storage for one second in room-temperature alkali vapor *Nat. Commun.* **9** 2074
[17] Höckel D, Scholz M and Benson O 2009 A robust phase-locked diode laser system for EIT experiments in cesium *Appl. Phys. B* **94** 429
[18] Davidson O, Yogev O, Poem E and Firstenberg O 2023 Single-photon synchronization with a room-temperature atomic quantum memory *Phys. Rev. Lett.* **131** 033601
[19] Kroh T *et al* 2019 Slow and fast single photons from a quantum dot interacting with the excited state hyperfine structure of the cesium D_1 -line *Sci. Rep.* **9** 1–11
[20] Vural H, Portalupi S L, Maisch J, Kern S, Weber J H, Jetter M, Wrachtrup J, Löw R, Gerhardt I and Michler P 2018 Two-photon interference in an atom-quantum dot hybrid system *Optica* **5** 367–73
[21] Maaß B, Barua A, Vincenz Ewald N, Robertson E, Gaur K, In Park S, Rodt S, Song J-D, Reitzenstein S and Wolters J 2025 Storage of single photons from a semiconductor quantum dot in a room-temperature atomic vapor memory with on-demand retrieval *Quantum Sci. Technol.* **10** 035058
[22] Thomas S E *et al* 2024 Deterministic storage and retrieval of telecom light from a quantum dot single-photon source interfaced with an atomic quantum memory *Sci. Adv.* **10** eadi7346
[23] van Loock P *et al* 2020 Extending quantum links: modules for fiber- and memory-based quantum repeaters *Adv. Quantum Technol.* **3** 1900141
[24] Pu Y-F, Zhang S, Wu Y-K, Jiang N, Chang W, Li C and Duan L-M 2021 Experimental demonstration of memory-enhanced scaling for entanglement connection of quantum repeater segments *Nat. Photon.* **15** 374–8
[25] Barrett S D, Rohde P P and Stace T M 2010 Scalable quantum computing with atomic ensembles *New J. Phys.* **12** 093032
[26] Zanin G L, Jacquet M J, Spagnolo M, Schiansky P, Calafell I A, Rozema L A and Walther P 2021 Fiber-compatible photonic feed-forward with 99% fidelity *Opt. Express* **29** 3425–37
[27] Akopian N, Wang L, Rastelli A, Schmidt O G and Zwiller V 2011 Hybrid semiconductor-atomic interface: slowing down single photons from a quantum dot *Nat. Photon.* **5** 230–3
[28] Reitzenstein S, Hofmann C, Gorbunov A, Strauß M, Kwon S H, Schneider C, Löffler A, Höfling S, Kamp M and Forchel A 2007 AlAs/GaAs micropillar cavities with quality factors exceeding 150.000 *Appl. Phys. Lett.* **90** 251109
[29] Schneider C, Heindel T, Huggenberger A, Weinmann P, Kistner C, Kamp M, Reitzenstein S, Höfling S and Forchel A 2009 Single photon emission from a site-controlled quantum dot-micropillar cavity system *Appl. Phys. Lett.* **94** 111111
[30] Moczała-Dusanowska M, Dusanowski Ł, Gerhardt S, He Y M, Reindl M, Rastelli A, Trotta R, Gregersen N, Höfling S and Schneider C 2019 Strain-tunable single-photon source based on a quantum dot–micropillar system *ACS Photon.* **6** 2025–31
[31] Rastelli A, Ulhaq A, Kiravittaya S, Wang L, Zrenner A and Schmidt O G 2007 In situ laser microprocessing of single self-assembled quantum dots and optical microcavities *Appl. Phys. Lett.* **90** 073120

[32] Mosor S, Hendrickson J, Richards B C, Sweet J, Khitrova G, Gibbs H M, Yoshie T, Scherer A, Shchekin O B and Deppe D G 2005 Scanning a photonic crystal slab nanocavity by condensation of xenon *Appl. Phys. Lett.* **87** 141105

[33] Dalacu D, Mnaymneh K, Sazonova V, Poole P J, Aers G C, Lapointe J, Cheriton R, SpringThorpe A J and Williams R 2010 Deterministic emitter-cavity coupling using a single-site controlled quantum dot *Phys. Rev. B* **82** 033301

[34] Srinivasan K and Painter O 2007 Optical fiber taper coupling and high-resolution wavelength tuning of microdisk resonators at cryogenic temperatures *Appl. Phys. Lett.* **90** 031114

[35] Maruf R A *et al* 2025 Reversible tuning of nanowire quantum dot to atomic transitions *ACS Photon.* **12** 4939–49

[36] Robert I, Moreau E, Gérard J M and Abram I 2001 Towards a single-mode single photon source based on single quantum dots *J. Lumin.* **94–95** 797–803

[37] Reithmaier J P, Sęk G, Löffler A, Hofmann C, Kuhn S, Reitzenstein S, Keldysh L V, Kulakovskii V D, Reinecke T L and Forchel A 2004 Strong coupling in a single quantum dot–semiconductor microcavity system *Nature* **432** 197–200

[38] Huwayz M A *et al* 2022 Optical properties of self-assembled InAs quantum dots based P–I–N structures grown on GaAs and Si substrates by molecular beam epitaxy *J. Lumin.* **251** 119155

[39] Benyoucef M, Rastelli A, Schmidt O G, Ulrich S M and Michler P 2006 Temperature dependent optical properties of single, hierarchically self-assembled GaAs/AlGaAs quantum dots *Nanoscale Res. Lett.* **1** 172

[40] Braun T, Betzold S, Lundt N, Kamp M, Höfling S and Schneider C 2016 Impact of ex situ rapid thermal annealing on magneto-optical properties and oscillator strength of In(Ga)As quantum dots *Phys. Rev. B* **93** 155307

[41] Dubowski J J, Stanowski R, Dalacu D and Poole P J 2018 Precision tuning of InAs quantum dot emission wavelength by iterative laser annealing *Opt. Laser Technol.* **103** 382–6

[42] Strauf S *et al* 2006 Frequency control of photonic crystal membrane resonators by monolayer deposition *Appl. Phys. Lett.* **88** 043116

[43] Bester G, Reuter D, He L, Zunger A, Kailuweit P, Wieck A D, Zeitler U, Maan J C, Wibbelhoff O and Lorke A 2007 Experimental imaging and atomistic modeling of electron and hole quasiparticle wave functions in InAs/GaAs quantum dots *Phys. Rev. B* **76** 075338

[44] Laferrière P *et al* 2023 Approaching transform-limited photons from nanowire quantum dots using excitation above the band gap *Phys. Rev. B* **107** 155422

[45] Maaß B, Ewald N V, Barua A, Reitzenstein S and Wolters J 2024 Room-temperature ladder-type optical memory compatible with single photons from semiconductor quantum dots *Phys. Rev. Appl.* **22** 044050

[46] Gorshkov A V, André A, Lukin M D and Sørensen A S 2007 Photon storage in Λ-type optically dense atomic media. II. Free-space model *Phys. Rev. A* **76** 033805

[47] Chen C *et al* 2024 Wavelength-tunable high-fidelity entangled photon sources enabled by dual stark effects *Nat. Commun.* **15** 5792

[48] Vural H, Portalupi S L and Michler P 2020 Perspective of self-assembled InGaAs quantum-dots for multi-source quantum implementations *Appl. Phys. Lett.* **117** 030501

[49] Jordan M, Androvitsaneas P, Clark R N, Trapalis A, Farrer I, Langbein W and Bennett A J 2024 Probing Purcell enhancement and photon collection efficiency of InAs quantum dots at nodes of the cavity electric field *Phys. Rev. Res.* **6** L022004

[50] Kim J-H, Richardson C J K, Leavitt R P and Waks E 2016 Two-photon interference from the far-field emission of chip-integrated cavity-coupled emitters *Nano Lett.* **16** 7061–6

[51] Gómez-López E, Meinecke M, Winkler K, Jurkat J, Huber-Loyola T, Hofling S and Benson O 2026 Data for Tuning of quantum dots in micropillar cavities for hybrid photonic interfaces [Data set] *Zenodo* (https://doi.org/10.5281/zenodo.18299647)